We are IntechOpen,
the world's leading publisher of
Open Access books
Built by scientists, for scientists

6,900
Open access books available

186,000
International authors and editors

200M
Downloads

Our authors are among the

154
Countries delivered to

TOP 1%
most cited scientists

12.2%
Contributors from top 500 universities

CLARIVATE ANALYTICS
BOOK CITATION INDEX
INDEXED

WEB OF SCIENCE™

Selection of our books indexed in the Book Citation Index
in Web of Science™ Core Collection (BKCI)

Interested in publishing with us?
Contact book.department@intechopen.com

Sintering Temperature Effect on Microstructure and Magnetic Evolution Properties with Nano- and Micrometer Grain Size in Ferrite Polycrystals

Raba'ah Syahidah Azis,
Muhammad Syazwan Mustaffa and
Nuraine Mariana Mohd Shahrani

Additional information is available at the end of the chapter

Abstract

The morphology and evolution of magnetic properties in multisample sintering (MSS) of yttrium iron garnet ($Y_3Fe_5O_{12}$, YIG) and single-sample sintering (SSS) of nickel zinc ferrite ($Ni_{0.6}Zn_{0.4}Fe_2O_4$, NZF) were studied in detail, focusing on the parallel evolving relationship with their dependences on sintering temperature. Sintering is an important process in ferrite fabrication which involved the process of transforming a noncrystalline powder into a polycrystalline solid by heating process. Under the influence of heat, the surface area is reduced through the formation and growth of bond between the particles associated with reduction in surface energy. This makes the particles move closer, grains to form by the movement of grain boundaries to grow over pores, and results in decreasing the porosity and increasing the density of the sample. Technological applications, especially in electronics applications, require high-density nanostructured ferrites, integrated by sintering from nanoparticles. The evolution from low to high sintering temperature will result in the transition from disordered to ordered ferromagnetism behavior. Multisample sintering (MSS) of yttrium iron garnet ($Y_3Fe_5O_{12}$, YIG) and single-sample sintering (SSS) of nickel zinc ferrite ($Ni_{0.6}Zn_{0.4}Fe_2O_4$, NZF) have been used as a studied material in this research work.

Keywords: MSS yttrium iron garnet ($Y_3Fe_5O_{12}$, YIG), SSS nickel zinc ferrite ($Ni_{0.6}Zn_{0.4}Fe_2O_4$, NZF), microstructure, magnetic properties

1. Introduction of garnet and spinel ferrites

Garnet ferrites with composition ($A_3B_5O_{12}$) structure have unique electromagnetic, magneto-optical, mechanical, and thermal properties [1]. Garnet ferrite comprises three crystallographic lattice (a, b, and c) sites. Among these lattice sites, the $24Fe^{3+}$, $16Fe^{3+}$, and $24R^{3+}$ ions occupy the [b] tetrahedral, (a) octahedral, and {c} dodecahedral sites, respectively, whereas oxygen ions are distributed to the interstitial sites [2]. However, R is the rare earth ions such as Ce, Gd, Y, and Nd. The general formula for rare earth garnets is $R_3Fe_5O_{12}$, whereas the ion distribution in rare earth garnets are $[Fe_2](Fe_3)\{R_3\}O_{12}$ represented tetrahedral, octahedral, and dodecahedral sites, respectively [3]. As for Ni-Zn ferrite, it has a spinel ferrite structure. Spinel ferrite crystallizes in the cubic structure. Spinels have the general formula $M(Fe_2O_4)$, where M is usually a divalent cation such as manganese (Mn^{2+}), nickel (Ni^{2+}), cobalt (Co^{2+}), zinc (Zn^{2+}), copper (Cu^{2+}), or magnesium (Mg^{2+}). The unit cell of spinel ferrites consists of 32 oxygen, 16 trivalent iron, and 8 divalent metal irons. The most important feature of the unit cell is that its array of oxygen ions leaves open two kinds of interstices, which can be filled by the metal ions. These interstices are referred to as tetrahedral or A sites and octahedral or B sites. The sintering process plays a prominent role in the fabrication of ceramics. Almost all ceramic bodies must be fired at elevated temperatures to produce a microstructure with the desired properties. This widespread use of sintering process has led to a variety of approaches to the subject. The criteria that should be met before sintering can occur are the mechanism for material transport and source of energy to activate and sustain this material transport. The relationship between microstructural properties with the effect of sintering temperature toward magnetic characteristics of MSS of yttrium iron garnet ($Y_3Fe_5O_{12}$, YIG) and SSS of nickel zinc ferrite ($Ni_{0.6}Zn_{0.4}Fe_2O_4$, NZF) is the focus of interest in this research work.

2. Brief overview of preparation methods

2.1. Preparation of hematite (Fe_2O_3)

About 100 g of mill scale was weighed using digital weighing balance. The mill scale was used as Fe_2O_3 source for preparing YIG. The mill scale was crushed by wet milling process for 48 h to obtain the precise sized powder. The magnetic particles were poured into a glass tube filled with 90–100°C distilled water in the presence of 1 T external magnetic field. Due to the weak susceptibility of ferromagnetic particles, FeO (wustite) presumably would drop to the bottom of the tube, and the Fe_3O_4 (magnetite) and Fe_2O_3 (hematite) would be attracted to the surface close to the poles. This separation was sorted out based on the Curie temperature of FeO, Fe_2O_3, and Fe_3O_4 particles [4, 5]. The one that has been used for Fe_2O_3 production is the bottom particles. The powder was oxidized using furnace at 500°C for 9 h in air. The yield of oxidation, Fe_2O_3, was sieving to obtain a fine powder and used as a raw material in preparing YIG.

### 2.2. Preparation and characterization of MSS of YIG

The starting raw powder materials of yttrium oxide (Y_2O_3) (99.9% purity, Alfa Aesar) and Fe_2O_3 which derived from mill scale (Curie separation technique) were mixed according to the stoichiometric ratio based on Eq. 1:

$$5Fe_2O_3 + 3Y_2O_3 \rightarrow 2Y_3Fe_5O_{12} \qquad (1)$$

The raw materials were mixed using an agate mortar for about 1 h. The mixing operation is necessary to combine the starting materials into a thoroughly homogeneous mixture. The mixing powder then was milled by using high-energy ball mill (SPEX8000D) with the ball to the powder weight ratio (BPR) of 10:1 for 9 h. After milling, polyvinyl alcohol with 1 wt.% PVA was added in the powder as a binder for giving strength to the pressed compact and was lubricated with 0.3 wt.% of zinc stearate. The mixture powder was pressed with 300 MPa into a toroidal shape. Then, the samples were sintered at different sintering temperatures from 500 to 1400°C for 9 h in air. The evolution of microstructural properties of the sample was determined by using a NovaNano 230 FESEM. The distribution of grain sizes was obtained by taking at least 200 different grain images and estimating the mean diameters of individual grains for each sample using J-image software. The magnetization studies were performed at room temperature using a LakeShore 7404 vibrating sample magnetometer with a maximum magnetic field of 11 kG. The variations of complex permeability were measured using an Agilent HP4291A Impedance Analyzer in the range of 1 MHz to 1.8 GHz.

2.3. Preparation and characterization of SSS of nickel zinc ferrite ($Ni_{0.6}Zn_{0.4}Fe_2O_4$, NZF)

The starting raw powder materials of nickel oxide (NiO), zinc oxide (ZnO), and iron oxide (Fe_2O_3) (>99% purity, Alfa Aesar) were mixed according to the stoichiometric ratio based on Eq. 2:

$$0.6NiO + 0.4ZnO + Fe_2O_3 \rightarrow Ni_{0.6}Zn_{0.4}Fe_2O_4 \qquad (2)$$
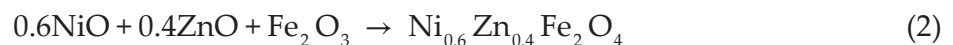
The mixed material was crushed by using a SPEX8000D HEBM machine at room temperature. The raw mixed powders were milled according to 10:1 ball to the powder weight ratio (BPR) for 6 h. The milled powder was granulated by using polyvinyl alcohol (1 wt.% PVA) as a binder and 0.1 wt. % zinc stearate was added as a lubricant. The previously granulated powder was then uniaxially pressed into toroidal form with pressure of 440 MPa. The single toroidal sample was repeatedly sintered from 600 up to 1200°C with an increment of 25°C under ambient air condition for 10 h. The evolution of microstructural properties of the sintered toroid was studied using a NovaNano 230 FESEM. The distribution of grain sizes was measured by taking at least 200 different grain images and estimating the mean diameters of individual grains for each sample using J-image software. The saturation induction, B_s, and coercivity, H_c, were determined from a *B-H* hysteresis loop which was obtained via a Linkjoin Technology MATS 2010SD Static Hysteresis graph. The frequency variations of the complex permeability were measured using an Agilent HP4291A Impedance Analyzer in the range of 1 MHz to 1.8 GHz.

3. Microstructure and magnetic properties of MSS yttrium iron garnet and SSS nickel zinc ferrite

3.1. MSS of yttrium iron garnet (YIG)

The samples undergo grain growth or the increase in size of grains when sintering at higher temperature. Sintering can be defined as removal of the pores between starting particles accompanied by shrinkage of the component combined with growth together and formation of strong bonds between adjacent particles [6, 7]. **Figure 1** shows the FESEM micrograph of samples sintered at different sintering temperatures. The micrograph of the sample sintered at 500, 600, and 700°C revealed that the sample encounters initial stage of sintering. The initial stage of sintering involves rearrangement of the powder particles and formation of strong bond or necks at the contact point between particles [8]. At 500 and 600°C, the sample showed nearly the same evolution trend, where the sample sintered at 500–600°C showed slight particle growth and rearrangement of the particles. After sintering at 700 and 800°C, the sample undergoes the formation of necks between particles. This can be noticed with the existence of dumbbell shape in the micrograph at these sintering temperatures. The red-dotted circles in **Figure 1** at 700°C indicate the necking structure between the particles. SEM micrograph of the samples sintered at 900, 1000, and 1100°C exhibits intermediate stage of sintering. Intermediate sintering is the stage where the size of the necks grows, the amount of porosity decreases substantially, and the particles move closer [9]. At this range of temperature, grain boundaries are formed and move so that some grains grew at the expense of others. Grain growth becomes increasingly active as the pore structure collapses. The pinning effect of the pore diminishes as they shrink and occupy less grain boundary area. Further sintering at 1200, 1300, and 1400°C corresponds to the final stage of sintering. The grains with the hexagonal structure are observed in this range of temperature. At this stage, the pores diminished and are slowly eliminated by diffusion of vacancies from the pores along the grain boundaries. The grain boundaries are regions of more open crystal structure than the grain themselves. Thus, the diffusion along grain boundary is more rapid. Reducing the grain boundary area by the grain growth lowers the energy of the system to a more stable state. From the results, it is believed that a mass transport mechanism started with atomic surface diffusion at relatively low temperature and continued to occur by the grain boundary diffusion, resulting in formation of necking, contact growth, pore elimination, and grain growth.

The magnetization versus magnetic field (M-H) curve of the sintered samples is measured at room temperature, as shown in **Figure 2**, and the corresponding saturation magnetization, M_s versus sintering temperature is given in **Table 1**. The saturation magnetization reached 0.597, 0.792, 0.259, and 0.069 emu/g at 500, 600, 700, and 800°C, respectively. These values could be related to the presence of weak ferromagnetic behavior of α-Fe_2O_3 and $YFeO_3$ and a significant amount of amorphous phase [10]. Moreover, such trend can also be associated with the mixture of disordered and ordered magnetism. The samples sintered from 500 to 800°C contained only weak magnetic phase as the magnetization in this temperature range is almost zero. It represents a very small amount of ordered magnetism in these samples. In addition, the smaller value of saturation magnetization in smaller grain size at this region temperature is attributed to the fine greater fraction of surface spins in the particles that tends to be canted with a smaller net moment. At 700 and 800°C, orthoferrites and hematite show
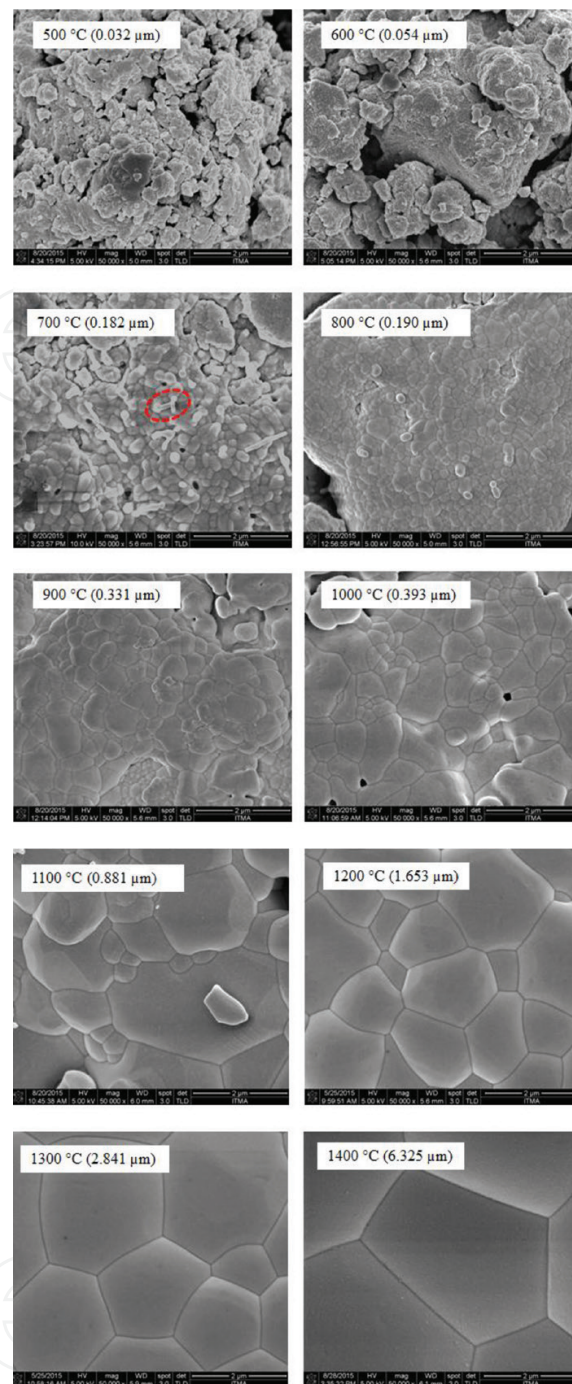
Figure 1. FESEM micrograph of MSS of YIG sintered from 500 to 1400°C.

the weak ferromagnetic behavior. The weak ferromagnetism arises from the low symmetry of the magnetic unit cell, producing a spin-canted structure of Fe sublattices. The weak ferromagnetic behavior of α-Fe_2O_3 is due to a slight disorder of the spin axis from exact antiparallelism. The increase in saturation magnetization for the sample sintered from 900 to 1100°C appears to be established by the initial formation of ferrimagnetic YIG phase at 900°C from the amorphous phase, while the sintering temperature at 1100°C shows only a single phase of YIG exist. This trend is characterized by a remarkable transformation from mixture of disordered and ordered to completely ordered arrangements of the magnetic moments in the sample.
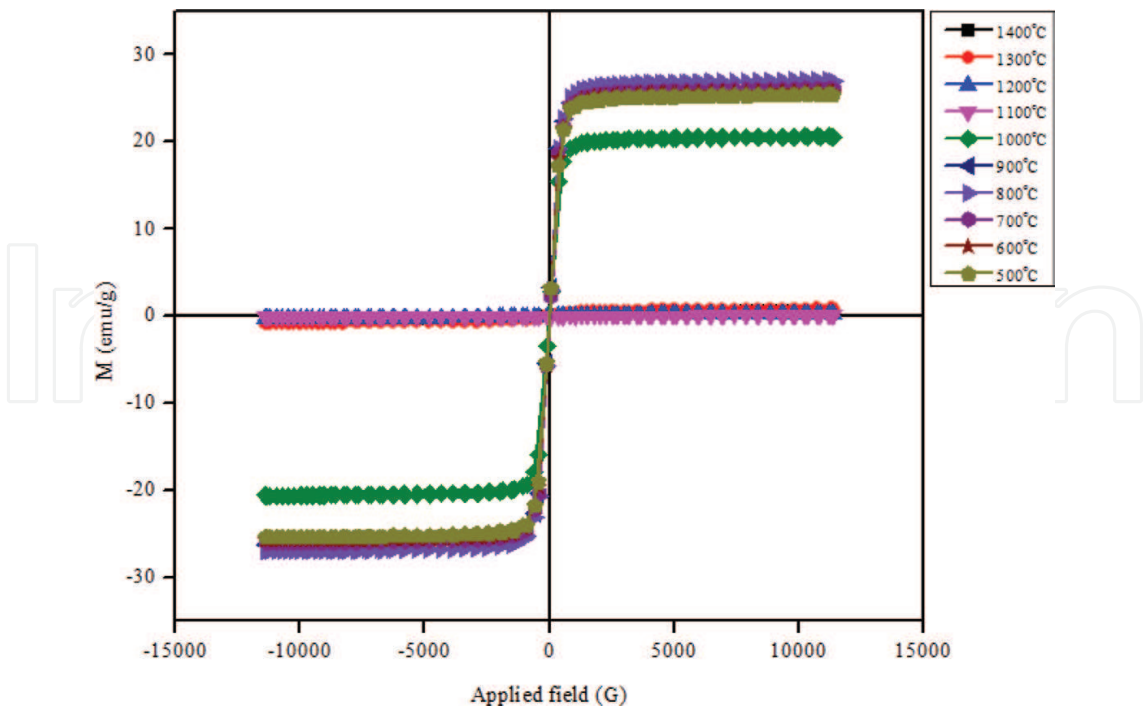
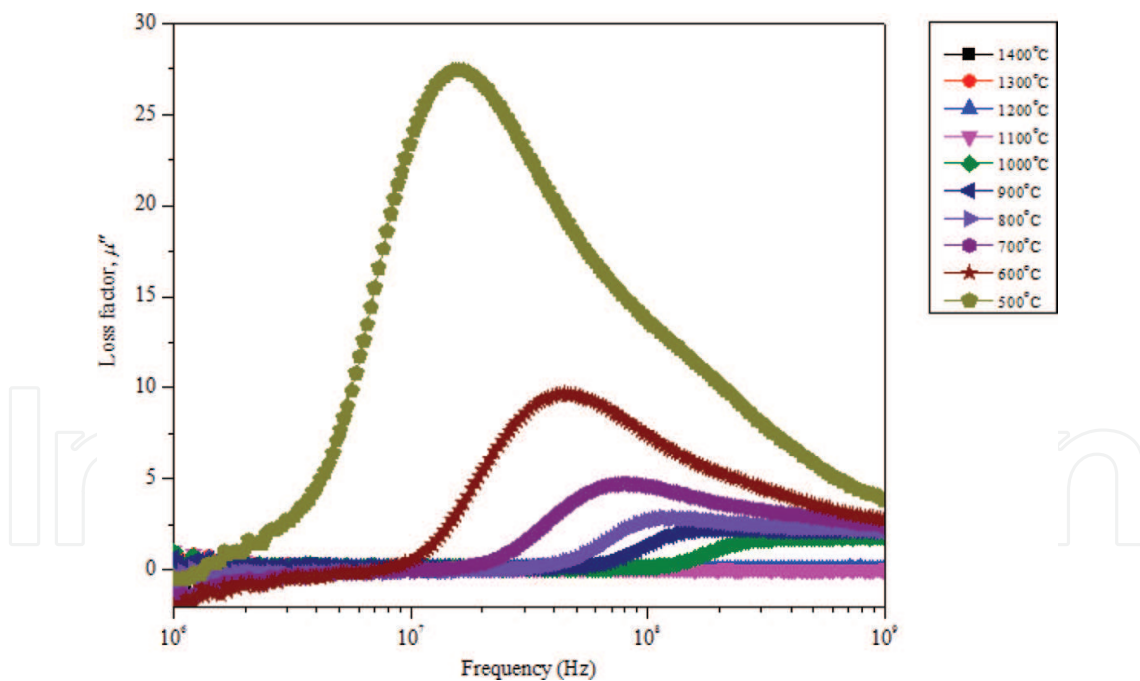**Figure 2.** Magnetization curve of MSS of YIG sintered from 500 to 1400°C.

Sintering Temperature (°C)	Saturation magnetization, M_s (emu/g)	Saturation magnetization, M_s (emu/cm³)	Coercivity, H_c (G)	Grain sizes (μm)
500	0.597	2.790	107.97	0.032
600	0.792	3.744	95.902	0.054
700	0.259	1.233	71.519	0.182
800	0.069	0.329	78.475	0.190
900	20.650	98.998	20.508	0.331
1000	26.282	126.322	8.564	0.393
1100	27.074	132.116	6.750	0.881
1200	26.086	127.550	3.605	1.653
1300	25.770	127.203	1.467	2.841
1400	25.466	130.157	3.715	6.325

Table 1. Saturation magnetization, M_s, and coercivity, H_c, of MSS of YIG sintered from 500 to 1400°C.

The sample sintered at 900°C exhibits the saturation magnetizations lower than the value of 26.8 emu/g, and at 1000°C, the saturation magnetization is close for the usual YIG ceramic, 26.8 emu/g [11]. This should be the contribution from the smallness of YIG present at 900°C and the basis of well-crystalline YIG with poor yttrium iron perovskite ($YFeO_3$) phase with high grain boundary content at 1000°C. The maximum saturation magnetization (27.074 emu/g) can be achieved at 1100°C. This value is higher as the amorphous phase is diminished due to the larger grain size and increasing bulk volume fraction of YIG. Thus, a strong interaction of magnetic moment within domains occurred due to exchange force. The powder sintered from 1200 to 1400°C shows a decreasing value of magnetization. The decrease of magnetization is
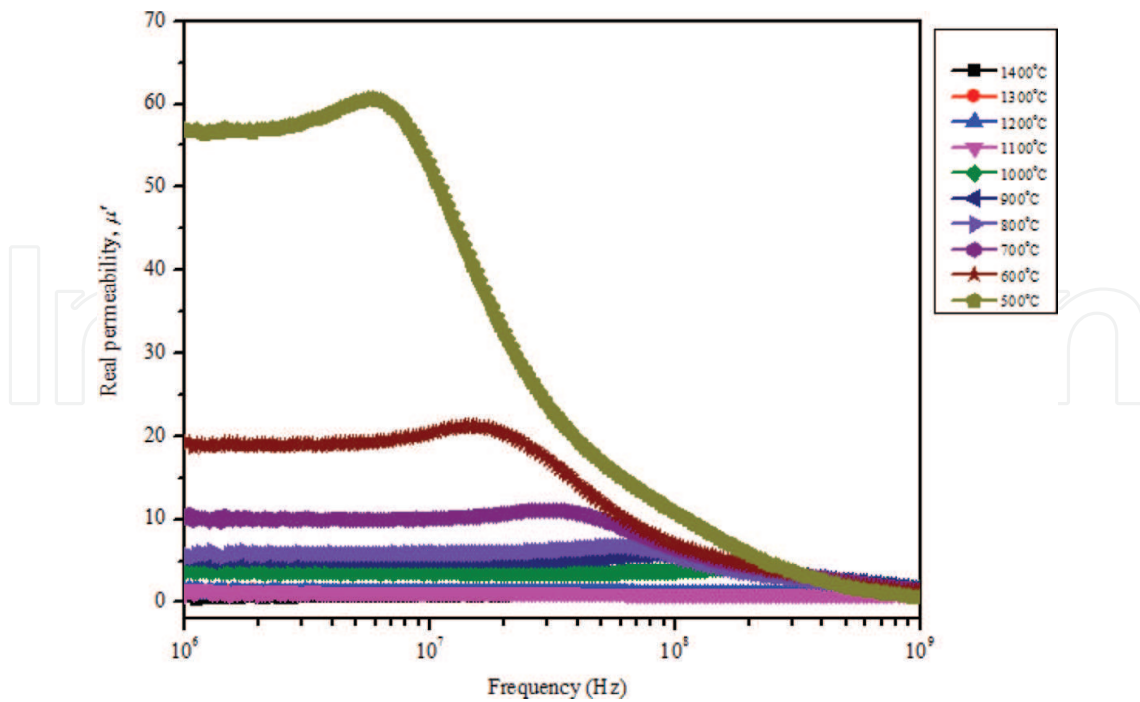
Figure 3. Real permeability, μ', of MSS of YIG sintered from 500 to 1400°C.

Figure 4. Loss factor, μ'', of MSS of YIG sintered from 500 to 1400°C.

mainly connected with oxygen gas surface interaction at higher sintering temperature. For larger grains, magnetization can follow the easy magnetization directions in the single grains, and domains can be formed within the grains. Thus, the magnetization process is determined by the magnetocrystalline anisotropy of the crystallites. For very small grains, ferromagnetic
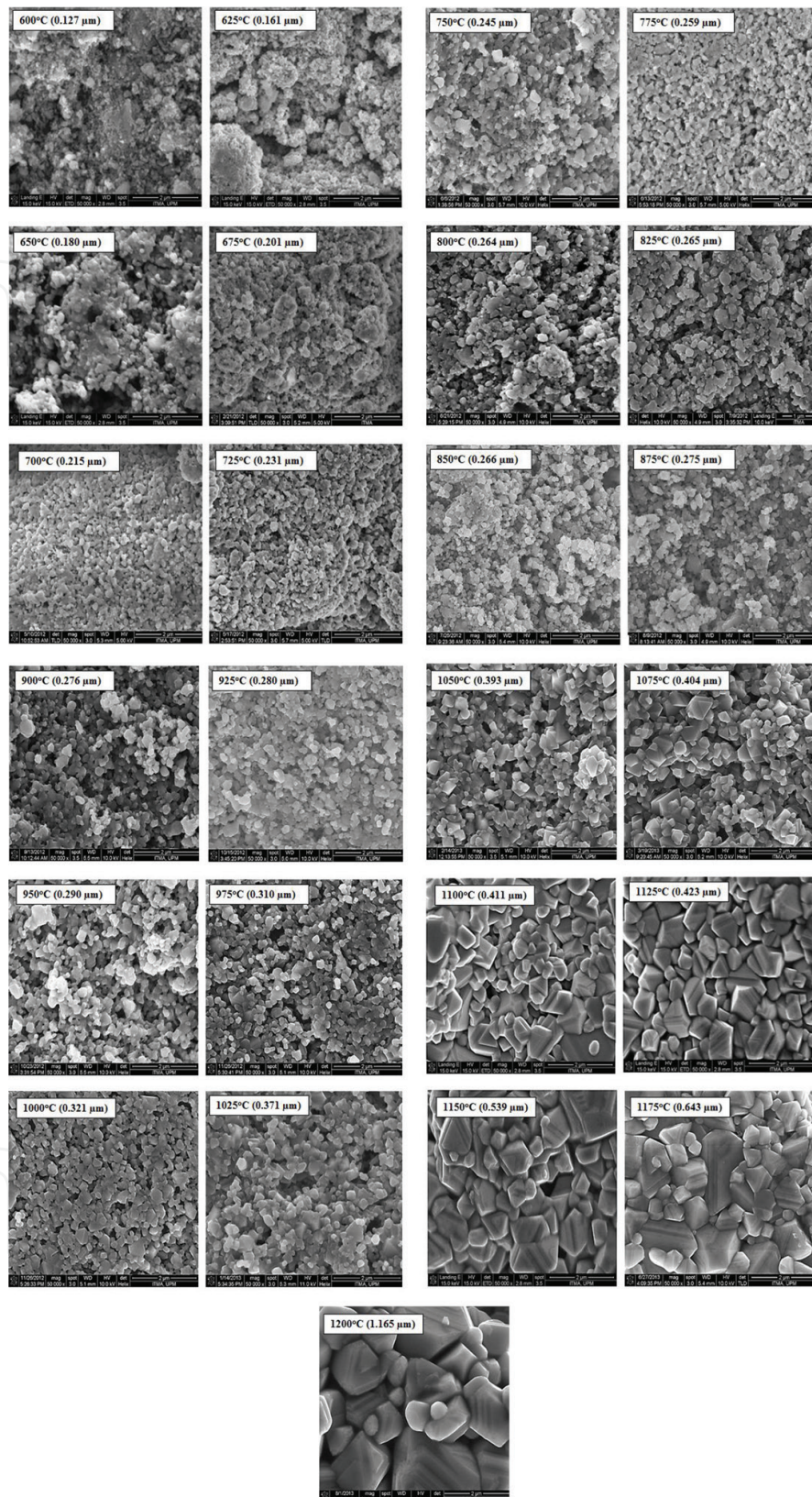
Figure 5. FESEM micrograph of SSS of $Ni_{0.6}Zn_{0.4}Fe_2O_4$ sintered from 600 to 1200°C.

exchange interaction more and more forces the magnetic moments to align parallel, thus impeding the magnetization to follow the easy direction of each individual grain.

Complex permeability consists of two components: the real permeability, μ', and loss factor, μ''. The room temperature of real permeability and loss factor of sintered samples are measured from 1.0 MHz to 1.8 GHz. The sample shows the μ' value is increased to a maximum value and then decreases rapidly to a very low value (**Figure 3**). The same trend of the loss factor is observed in **Figure 4**. The samples show the increment of permeability loss factor with the rise in frequency and attain the maximum value at particular frequency and decrease with further increase in frequency. From both figures (**Figures 3** and **4**), it can be seen that the μ'' maximizes, while the μ' drops off at 10 MHz because of the occurrence of a magnetic resonance. The sample sintered at 500–800°C has low values of the real permeability and does not show the trend of permeability as same as the higher temperature because of the presence of amorphous phase. The increase of μ' value with sintering temperature after 900°C and above is due to the increasing of grain sizes which correspondingly reduce the grain boundaries inside the sample. As the crystallinity and phase purity increase with increasing sintering temperature, the magnetic mass is increased and makes the movement of the domain wall easier. The increase in the sintering temperature also results in the decrease of magnetic anisotropy by decreasing the internal stress and crystal anisotropy [12]. Hence, the hindrance of the movement of domain wall is reduced and increases the value of μ'.

The loss factor, μ'', is the imaginary part of initial permeability. The permeability loss factor arises due to the lag between the magnetization or flux induction and external applied field [6]. The main types of losses encounter in ferrites are the hysteresis loss, eddy current loss, and residual loss. Otsuki et al. [13] reported that the larger grain size increases the eddy current loss because of the easier movement of domain wall in the larger grain. The fraction of larger grains that are occupied with domain wall also increases hysteresis losses. Hysteresis loss can be minimized if one reduces the hindrance to the domain wall motion by reducing the pinning center to the domain wall movement such as volume fraction of pores, impurities and dislocations, and internal strain inside the sample. The hysteresis loss becomes less important in the high-frequency range due to spin rotation at higher frequency. The eddy current loss is important at higher frequency because of the circulating current induced in the sample due to the change of magnetic field which leads to the energy losses. However, in the polycrystalline YIG, the eddy current losses can be neglected due to high resistivity of YIG. Residual loss is also important in the high-frequency range. To reduce the residual loss, the complex permeability has to be made to peak at the high frequency as possible by using fine-grained sample.

3.2. SSS of nickel zinc ferrite ($Ni_{0.6}Zn_{0.4}Fe_2O_4$)

SEM micrographs for single-sample sintering (SSS) of $Ni_{0.6}Zn_{0.4}Fe_2O_4$ are shown in **Figure 5**. The increased average grain size shows the microstructural evolution of the sample. The microstructural evolution can be described by adapting the stages of sintering which are three major stages involved in this process:

i. Initial stage sintering involves rearrangement of the powder particles and formation of a strong bond or neck at the contact points between particles [14].

ii. Sample sintered from 600 to 1050°C shows an intermediate stage of sintering, where the size of the neck grows, the amount of porosity decreases substantially, and particles move closer leading to shrinkage of the component. Grain boundaries and grains are formed and move so that some grains grow at the expense of others. This stage continues while the pore channels are connected (open porosity) but is considered over when the pores are isolated (closed porosity).

iii. Final stage sintering occurred in the sample sintered from 1075 to 1200°C. In this stage, the pores become closed and are slowly eliminated generally by diffusion of vacancies from the pores along grain boundaries with only a little densification of the component. The grain boundaries are regions of more open crystal structure than the grains themselves so that diffusion along them is more rapid. Grain size increases during this stage.

The developments of *B-H* hysteresis loops are shown in **Figure 6**. The hysteresis properties of polycrystalline nickel zinc ferrite (**Table 2**) are very sensitive to the structure and volume fraction of the complete phase, and also to the grain size. The trends of loops are discussed below:

i. 600–1000°C: narrowly bulging but linear-looking shape which consists of weak ferromagnetic phase + paramagnetic phase (amorphous phase) + superparamagnetic phase (crystalline phase and small particles). At this stage, the hysteresis shape is significantly dominated by paramagnetic phase because it does not show the properties associated with ordered magnetism. It shows very slight hysteresis with low saturation induction, B_s indicating the low degree of crystallinity and a small amount of ferromagnetic phase. The magnetic moments begin to line up in the direction of applied field with a complex process such as domain growth, domain walls motion, and domain rotation [15–18].

ii. 1025–1125°C: slanted sigmoid shape which consists of moderate ferromagnetic phase + paramagnetic phase. As sintering temperature increased, paramagnetic states decreased, and at 1025°C, a moderately ferromagnetic state appeared. With further sintering, there is an increase in the volume fraction of grains, yielding more magnetic crystalline mass which would exhibit stronger ferromagnetism with negligible paramagnetic phase (amorphous phase) arising from nickel zinc ferrite phase formation. They have higher B_s values indicating that higher ferromagnetic phase crystallinity is formed [15–18].

iii. 1150–1200°C: erect, narrower, and well-defined sigmoid shape which consists of strong ferromagnetic phase. At this stage, strong ferromagnetism state was very dominant with negligible superparamagnetism and paramagnetism due to their high volume fraction of the complete Ni-Zn ferrite phase, high density, large grain size, and low amount of microstructure defects which allow easy domain wall movement in the magnetization and demagnetization process [15–18].

Figure 7 shows the real permeability, μ' results plotted against the frequency in the range of 1.0 MHz to 1.8 GHz. The real permeability remains almost unchanged at low frequency, rises

slightly, and then drops sharply when the frequency gets to a certain high value, which is called the cutoff frequency. The magnetic permeability and the cutoff frequency, f_o, confirm the Snoek's relation [19] by using Eq. 3:

$$\mu_i f_o = \text{Constant} \tag{3}$$

The real permeability increase with sintering temperature can be attributed to increase in density and grain size with sintering temperature [20]. At higher sintering temperature, with increased grain size, a fewer number of grain boundaries would be present, and diminished grain boundary caused the existence of very mobile domain walls thus increasing the permeability value of the $Ni_{0.6}Zn_{0.4}Fe_2O_4$. During grain growth, pores become fewer which act as barrier to domain wall motion due to pinning of the wall. Besides that, the increase in sintering temperature results in a decrease of the magnetic anisotropy by decreasing the internal stress and crystal anisotropy, which reduces the hindrance to the motion of domain walls [17, 21–23].

The same trend is seen in the case of variation in loss factor, μ'', with respect to frequency as shown in **Figure 8**. The loss factor was observed first to remain constant with frequency, attain the maximum value at a particular frequency, and then decrease with increase in frequency. The loss factor increased with the increasing sintering temperature and grain size. When the grain size increases, more domain walls exist in the grain. Therefore, the domain walls can move easily in the larger grain. When the grain is large, which means a
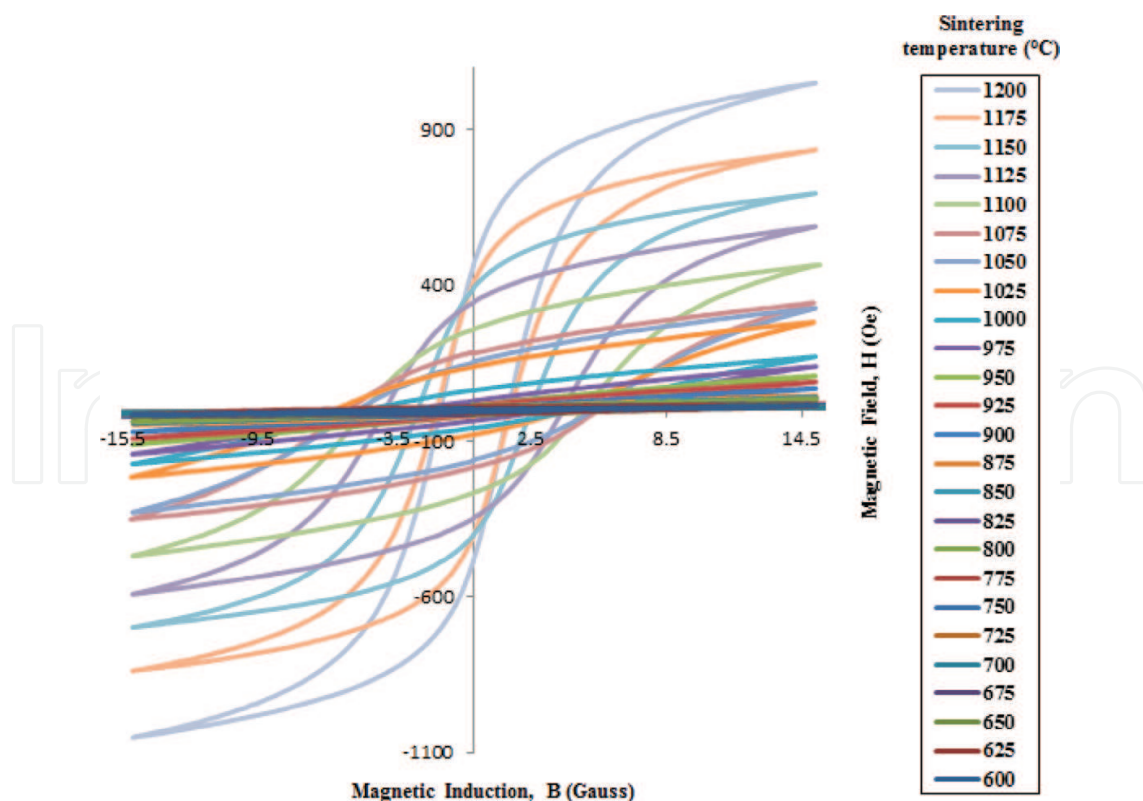
Figure 6. B-H hysteresis loop of SSS of $Ni_{0.6}Zn_{0.4}Fe_2O_4$ sintered at 600 to 1200°C.

Sintering temperature (°C)	Average grain size, D (μm) (±0.01 μm)	Saturation induction, B_s (Gauss) (±5 G)	Coercivity, H_c (Oe) (±0.01 Oe)
600	0.127	16.96	1.38
625	0.161	17.08	1.81
650	0.180	18.22	1.92
675	0.201	19.22	2.00
700	0.215	20.90	2.02
725	0.231	21.20	2.13
750	0.245	24.64	2.29
775	0.259	32.84	2.84
800	0.264	36.65	2.99
825	0.265	37.36	3.11
850	0.266	42.20	3.17
875	0.275	46.56	3.21
900	0.276	69.83	3.37
925	0.280	91.11	3.44
950	0.290	110.10	3.58
975	0.310	141.10	3.82
1000	0.321	172.50	4.58
1025	0.371	248.90	5.13
1050	0.393	328.20	5.20
1075	0.404	348.00	5.32
1100	0.411	467.70	4.84
1125	0.423	590.50	3.98
1150	0.539	697.50	2.50
1175	0.643	837.50	1.60
1200	1.165	1052.00	1.33

Table 2. Average grain size, saturation induction, B_s, and coercivity, H_c, of SSS of $Ni_{0.6}Zn_{0.4}Fe_2O_4$ sintered from 600 to 1200°C.
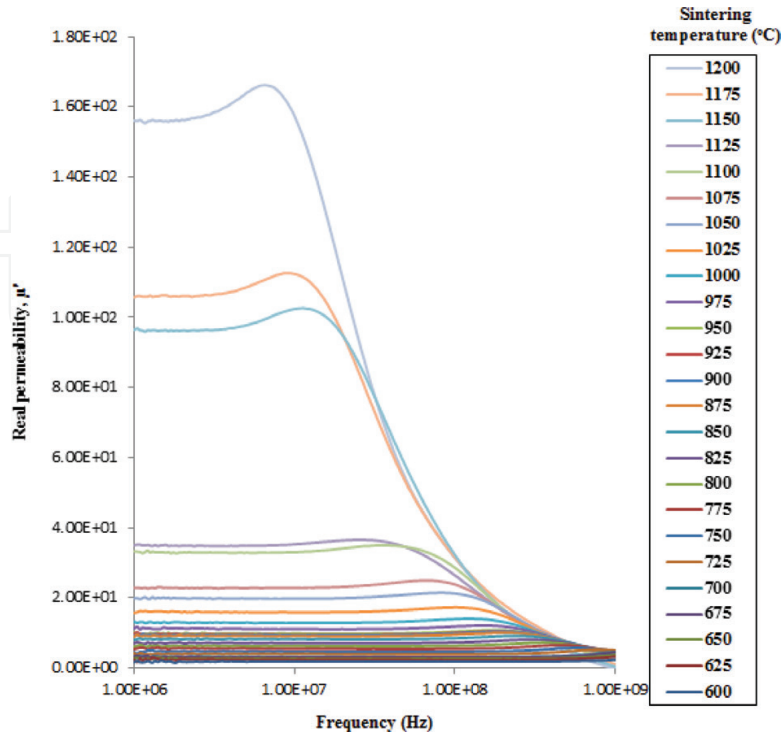
Figure 7. Real permeability, μ', of SSS of $Ni_{0.6}Zn_{0.4}Fe_2O_4$ sintered from 600 to 1200°C.
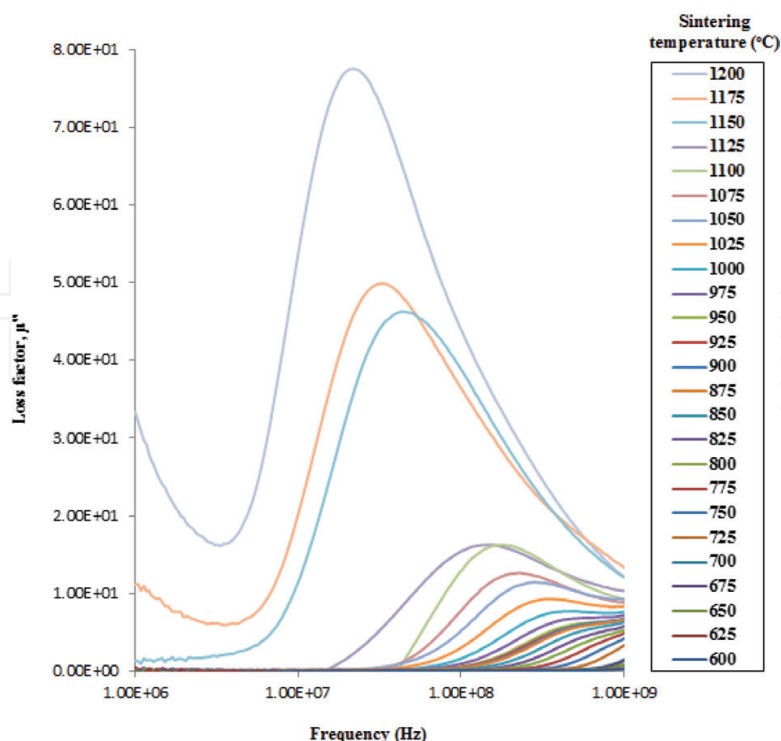
Figure 8. Loss factor, μ'', of SSS of $Ni_{0.6}Zn_{0.4}Fe_2O_4$ sintered from 600 to 1200°C.

decrease in the number of grain boundaries; it will not strongly impede the eddy current flows. Thus, larger eddy current is induced [17, 23–25]. Usually, small grains with prominent grain boundaries lead to higher resistivity, the eddy current loss of which is negligible. The losses in ferrites are associated with rotational resonance and domain wall relaxation. Rotational resonance is usually observed at higher frequencies, while domain wall relaxation is observed at lower frequencies [12, 26, 27]. The major contribution to the magnetic losses in ferrites is due to hysteresis losses, which are based on the damping phenomena associated with spin rotations and irreversible wall displacement. In the high-frequency range, the hysteresis losses become less important because the wall displacement is mainly damped and the losses would be mos due to spin rotation [13, 22, 28]. Comparing **Figures 7** and **8**, it is observed that the off-resonance frequency region of μ'' firstly occurred and was later followed by the μ''. The lag in this process was due to μ' being in phase with the external field, whereas μ'' was out of phase with the external field [29].

4. Conclusion

MSS YIG and SS NZF have been prepared via mechanical alloying technique. The samples were sintered at various sintering temperatures in order to study the influence of sintering temperatures on the microstructure and magnetic properties. Increasing sintering temperature will enhance the grain size with less grain boundaries. This extrinsically increases the real magnetic permeability, μ', loss factor, μ'', and the saturation magnetization, M_s. The higher magnetic permeability represents the high frequency losses due to the presence of grain boundaries as impediments to domain wall motion. The large M_s reduces the coercivity,

H_c as the increasing the multidomain grain size. The magnetic hysteresis and complex permeability graph can be categorized into three distinct groups which represent the formation of a paramagnetic state to a moderate ferromagnetic state and then to a strong ferromagnetic state with microstructural changes at varied sintering temperatures.

Acknowledgements

Author details

Raba'ah Syahidah Azis[1,2]*, Muhammad Syazwan Mustaffa[1] and
Nuraine Mariana Mohd Shahrani[2]

*Address all correspondence to: rabaah@upm.edu.my

1 Department of Physics, Faculty of Science, Universiti Putra Malaysia, UPM, Serdang, Selangor, Malaysia

2 Materials Synthesis and Characterization Laboratory (MSCL), Institute of Advanced Technology, Universiti Putra Malaysia, UPM, Serdang, Selangor, Malaysia

References

[1] Joseyphus RJ, Narayanasamy A, Nigam AK, Krishnan R. Effect of mechanical milling on the magnetic properties of garnets. Journal of Magnetism and Magnetic Materials. 2006;**296**:57-64. DOI: 10.1016/j.jmmm.2005.04.018

[2] Park MB, Cho NH. Structural and magnetic characteristics of yttrium iron garnet (YIG, Ce:YIG) films prepared by RF magnetron sputter techniques. Journal of Magnetism and Magnetic Materials. 2001;**231**:253-264. DOI: 10.1016/S0304-8853(01)00068-3

[3] Xu H, Yang H, Xu W, Feng S. Magnetic properties of Ce, Gd substituted yttrium iron garnet ferrite powders fabricated using a sol–gel method. Journal of Materials Processing Technology. 2008;**197**:296-300. DOI: 10.1016/j.jmatprotec.2007.06.061

[4] Azis RS, Hashim M, Saiden NM, Daud N, Shahrani NN. Study the iron environments of the steel waste product and its possible potential applications in ferrites. Advances in Materials Research. 2015;**1109**:295-299. DOI: 10.4028/www.scientific.net/AMR.1109.295

[5] Azis RS, Hashim M, Yahya N. High purity iron oxide a-Fe_2O_3 from mill scale using Curie temperature separation technique (2002). Journal of Solid State Science and Technology. 2002;**9**(1):87-90

[6] Paladino AE, Maguire EA. Microstructure development in yttrium iron garnet. Journal of the American Ceramic Society. 1970;**53**(2):98-102. DOI: 10.1111/j.1151-2916.1970.tb12019.x

[7] Heister W. Magnetic properties and grain structure of Mn-Zn ferrites. Journal of Applied Physics. 1959;**30**:22-24. DOI: 10.1063/1.2185902

[8] Shahrani NMM, Azis RS, Hashim M, Hassan J, Zakaria A, Daud N. Effect of variation sintering temperature on magnetic permeability and grain sizes of $Y_3Fe_5O_{12}$ via mechanical alloying technique. Materials Science Forum. 2015;**846**:395-402. DOI: 10.4028/www.scientific.net/MSF.846.395.

[9] Shahrani NMM, Azis RS, Hashim M, Hassan J, Abbas Z, Daud N, Sulaiman S, Muda NNC, Azizan AAH, Musa MA. Effect of sintering temperature on crystallography and microstructure of yttrium iron garnet via mechanical alloying technique. Journal of Solid State Science and Technology Letters. 2015;**16**(1-2):67-72

[10] Musa MA, Azis RS, Osman NH, Hassan J, Dihom MM. Structural and magnetic properties of yttrium aluminum iron garnet (YAlG) nanoferrite prepared via auto-combustion sol–gel synthesis. Journal of the Australian Ceramic Society. 2018;**54**(1):55-63. DOI: 10.1007/s41779-017-0126-7

[11] Huang H, Gong H, Tang D, Tan OK. Synthesis and characterization of yttrium aluminum garnet by high-energy ball milling. Optical Materials. 2009;**31**:716-719. DOI: 10.1016/j.optmat.2008.07.006

[12] Nazlan R, Hashim M, Abdullah NH, Ibrahim IR, Ismail I. Influence of milling time on the crystallization, morphology and magnetic properties of polycrystalline yttrium iron garnet. Advanced Materials Research. 2012;**501**:324-328. DOI: 10.4028/www.scientific.net/AMR.501.324

[13] Zhao H, Zhou J, Bai Y, Gui Z, Li L. Effect of bi-substitution on the dielectric properties of polycrystalline yttrium iron garnet. Journal of Magnetism and Magnetic Materials. 2004;**280**:208-213. DOI: 10.1016/j.jmmm.2004.03.014

[14] Azizi A, Sadrnezhaad SK. Effects of annealing on phase evolution, microstructure and magnetic properties of mechanically synthesized nickel-ferrite. Ceramics International. 2010;**36**:2241-2245. DOI: 10.1016/j.ceramint.2010.06.004

[15] Idza IR, Hashim M, Rodziah N, Ismayadi I, Norailiana AR. Influence of evolving microstructure on magnetic-hysteresis characteristics in polycrystalline nickel-zinc ferrite $Ni_{0.3}Zn_{0.7}Fe_2O_4$. Materials Research Bulletin. 2012;**47**:1345-1352. DOI: 10.1016/j.materresbull.2012.03.007

[16] Ismayadi I, Hashim M, Khamirul AM, Alias R, Hassan J. The transition from paramagnetic to ferromagnetic states as influenced by evolving microstructure of $Ni_{0.5}Zn_{0.5}Fe_2O_4$. Journal of Superconductivity and Novel Magnetism. 2012;**25**(1):71-77. DOI: 10.1007/s10948-011-1201-x

[17] Ismail I, Hashim M, Kanagesan S, Ibrahim IR, Nazlan R, Wan Ab Rahman WN, Abdullah NH, Mohd Idris F, Bahmanrokh G, Shafie MSE, Manap M. Evolving microstructure, magnetic properties and phase transition in a mechanically alloyed $Ni_{0.5}Zn_{0.5}Fe_2O_4$ single sample. Journal of Magnetism and Magnetic Materials. 2014;**351**:16-24. DOI: 10.1016/j.jmmm.2013.09.041

[18] Mustaffa MS, Hashim M, Azis RS, Ismail I, Kanagesan S, Zulkimi MM. Magnetic phase-transition dependence on nano-to-micron grain-size microstructural changes of mechanically alloyed and sintered $Ni_{0.6}Zn_{0.4}Fe_2O_4$. Journal of Superconductor and Novel Magnetism. 2014;**27**:1451-1462. DOI: 10.1007/s10948-013-2453-4

[19] Goldman A. Modern Ferrite Technology. New York: Van Nostraud Reinhold; 1990

[20] Nakamura TO. Electromagnetic properties of Mn–Zn ferrite sintered ceramics. Journal of Applied Physics. 1996;**79**:7129-7233. DOI: 10.1063/1.361482

[21] Verma A, Goel TC, Mendiratta RG. Frequency variation of initial permeability of Ni-Zn ferrites prepared by the citrate precursor method. Journal of Magnetism and Magnetic Materials. 2000;**210**:274-278. DOI: 10.1016/S0304-8853(99)00451-5

[22] Ismayadi I, Hashim M. Sintering temperature dependence of evolving morphologies and magnetic properties of $Ni_{0.5}Zn_{0.5}Fe_2O_4$ synthesized via mechanical alloying. Journal of Superconductivity and Novel Magnetism. 2012;**25**:1551-1561. DOI: 10.1007/s10948-012-1468-6

[23] Jahanbin T, Hashim M, Khamirul AM, Waje SB. Influence of sintering temperature on the structural, magnetic and dielectric properties of $Ni_{0.8}Zn_{0.2}Fe_2O_4$ synthesized by co-precipitation route. Journal of Alloys and Compounds. 2010;**503**:111-117. DOI: 10.1016/j.jallcom.2010.04.212

[24] Waje SB, Hashim M, Wan Yusoff WD, Abbas Z. Sintering temperature dependence of room temperature magnetic and dielectric properties of $Co_{0.5}Zn_{0.5}Fe_2O_4$ prepared using mechanically alloyed nanoparticles. Journal of Magnetism and Magnetic Materials. 2010;**322**:686-691. DOI: 10.1016/j.jmmm.2009.10.041

[25] Jahanbin T, Hashim M, Matori KA. Comparative studies on the structure and electromagnetic properties of Ni-Zn ferrites prepared via co-precipitation and conventional ceramic processing routes. Journal of Magnetism and Magnetic Materials. 2010;**322**:2684-2689. DOI: 10.1016/j.jmmm.2010.04.008

[26] Vajargah SH, Hosseini HRM, Nemati ZA. Preparation and characterization of nanocrystalline misch-metal-substituted yttrium iron garnet powder by the sol–gel combustion process. International Journal of Applied Ceramic Technology. 2008;**5**:464 468. DOI: 10.1111/j.1744-7402.2008.02241.x

[27] Goldman A. Modern Ferrite Technology. Pittsburgh: Springer Science and Business Media, Inc; 2006

[28] Verma A, Chatterjee R. Effect of zinc concentration on the structural, electrical and magnetic properties of mixed Mn-Zn and Ni-Zn ferrites synthesized by the citrate precursor technique. Journal of Magnetism and Magnetic Materials. 2006;**306**:313-320. DOI: 10.1016/j.jmmm.2006.03.033

[29] Goldman A. Handbook of Modern Ferromagnetic Materials. Massachusetts: Kluwer Academic Publishers; 1999